

CHANDRA PULSAR SURVEY (CHAPS).

OLEG KARGALTSEV¹, MARTIN DURANT¹, GEORGE G. PAVLOV^{2,3}, AND GORDON GARMIRE²

Draft version March 8, 2018

ABSTRACT

Taking advantage of the high sensitivity of the *CXO* Advanced CCD Imaging Spectrometer, we have conducted a snap-shot survey of pulsars previously undetected in X-rays. We detected 12 pulsars and established deep flux limits for 11 pulsars. Using these new results, we revisit the relationship between the X-ray luminosity, L_X^{psr} , and spin-down power, \dot{E} . We find that the obtained limits further increase the extremely large spread in the non-thermal X-ray efficiencies, $\eta_X^{\text{psr}} = L_X^{\text{psr}} / \dot{E}$, with some of them being now below 10^{-5} . Such a spread cannot be explained by poorly known distances or by beaming of pulsar radiation. We also find evidence of a break in the dependence of L_X^{psr} on \dot{E} , such that pulsars become more X-ray efficient at $\dot{E} \lesssim 10^{34} - 10^{35} \text{ erg s}^{-1}$. We examine the relationship between the γ -ray luminosity, L_γ^{psr} , and \dot{E} , which exhibits a smaller scatter compared to that in X-rays. This confirms that the very large spread in the X-ray efficiencies cannot be explained just by the beaming because the γ -ray emission is generally expected to be beamed stronger than the X-ray emission. Intriguingly, there is also an indication of a break in the $L_\gamma^{\text{psr}}(\dot{E})$ dependence at $\dot{E} \sim 10^{35} \text{ erg s}^{-1}$, with lower- \dot{E} pulsars becoming less γ -ray efficient. We also examine the distance-independent $L_\gamma^{\text{psr}} / L_X^{\text{psr}}$ ratio as a function of \dot{E} for a sample of γ -ray pulsars observed by *CXO* and find that it peaks at $\dot{E} \sim 10^{35} \text{ erg s}^{-1}$, showing that the breaks cannot originate from poorly measured distances. We discuss the implications of our findings for existing models of magnetospheric emission and venues for further exploration.

Subject headings: X-rays: general, pulsars: general

1. INTRODUCTION

Along with observations in the radio band, X-rays have been the primary spectral window to study rotation-powered pulsars. Thanks to their superb sensitivity and angular resolution, the latest generation X-ray telescopes have detected emission from $\gtrsim 100$ rotation-powered isolated pulsars and about 60 pulsar-wind nebulae (PWNe; Kargaltsev & Pavlov 2008, 2010; hereafter KP08 and KP10). The growing sample allows one to look for dependences between the X-ray properties and other pulsar parameters, such as the pulsar rotational energy loss rate (spin-down power) \dot{E} .

There have been multiple attempts to establish the relationship between the pulsar X-ray luminosity, L_X^{psr} , and \dot{E} , including those based on *Einstein* data ($L_X^{\text{psr}} \propto \dot{E}^{1.39}$; Seward & Wang 1988), *ROSAT* data ($L_X^{\text{psr}} \sim 10^{-3} \dot{E}$; Becker & Trümper 1997), *ASCA*, *RXTE*, *Bep-poSAX*, *CXO*, and *XMM-Newton* data ($L_X^{\text{psr}} \propto \dot{E}^{1.34}$; Possenti et al. 2002), *CXO* and *XMM-Newton* data ($L_X^{\text{psr}} \propto \dot{E}^{0.92}$; Li et al. 2008), and *CXO* data (KP08).

One of the reasons for such a variety of scaling relations is the different approaches used by different authors. For instance, they used different energy ranges, different con-

tribution of extended PWN emission (because of the limited telescope resolution), and some of them did not isolate the nonthermal magnetospheric emission from a possible thermal component (generally seen below $\sim 2 \text{ keV}$). Nonetheless, Possenti et al. (2002) have already pointed out that the best-fit relation does not provide a statistically acceptable fit to the data due to the very large scatter in L_X^{psr} for pulsars with similar \dot{E} values and noted that all L_X^{psr} points appear to lie below the curve (upper bound) given by $L_{X,\text{crit}}^{\text{psr}} \propto \dot{E}^{1.48}$. This conclusion was strengthened by KP08 who collected the results of *CXO* observations of ~ 40 pulsars and their PWNe and found $L_{X,\text{crit}}^{\text{psr}} \propto \dot{E}^{1.3}$ and $L_{X,\text{crit}}^{\text{pwn}} \propto \dot{E}^{1.6}$ (generally consistent with Possenti et al. 2002, who did not separate the pulsar and PWN contributions).

After the launch of the *Fermi* γ -ray observatory, the number of γ -ray detected pulsars has grown rapidly, and it has nearly matched the number of X-ray detected pulsars after three years of LAT operation⁴. The achieved progress makes it possible to carry out studies similar to those in X-rays. In particular, Marelli et al. (2011) have studied both X-ray and γ -ray properties of 29 *Fermi* pulsars with well-characterized X-ray spectra. From analyzing the X-ray properties of these pulsars, Marelli et al. (2011) found the best-fit correlation $L_X^{\text{psr}} \propto \dot{E}^{1.04}$, albeit again with a large scatter, which made this fit formally unacceptable. The best-fit correlation for the γ -ray luminosity, $L_\gamma^{\text{psr}} \propto \dot{E}^{0.88}$, also resulted in a poor fit. However,

¹ Department of Astronomy, University of Florida, Gainesville, FL 32611–2055, USA; martin.durant@astro.ufl.edu, oyk100@astro.ufl.edu

² Department of Astronomy and Astrophysics, Pennsylvania State University, University Park, PA 16802, USA; pavlov@astro.psu.edu

³ St.-Petersburg State Polytechnical University, Polytekhnikeskaya ul. 29, 195251, Russia

⁴ See <https://confluence.slac.stanford.edu/display/GLAMCOG/Public+List+Detected+Gamma-Ray+Pulsars>

in this case the poor quality of the fit could be caused by an apparent break at $\dot{E}_{\text{crit}} \approx 3.7 \times 10^{35} \text{ erg s}^{-1}$ rather than just by the scatter. Above \dot{E}_{crit} , the best fit relation appears to be $L_{\gamma}^{\text{psr}} \propto \dot{E}^{0.2}$ while it is $L_{\gamma}^{\text{psr}} \propto \dot{E}^{1.43}$ below \dot{E}_{crit} . Marelli et al. (2011) also considered the dependence of the distance-independent $L_{\gamma}^{\text{psr}}/L_{\text{X}}^{\text{psr}}$ ratio on \dot{E} and found that the ratio shows a strong scatter (up to 3 orders of magnitude) and a very weak (or no) correlation with \dot{E} (see Figure 4 of Marelli et al. 2011). The scatter in $L_{\gamma}^{\text{psr}}/L_{\text{X}}^{\text{psr}}$ could simply be caused by the scatter in $L_{\text{X}}^{\text{psr}}$.

In this paper we present analysis based on the largest reported sample of isolated, rotation-powered pulsars observed by the Advanced CCD Imaging Spectrometer (ACIS) aboard *CXO*. The advantage of *CXO*/ACIS is that even within a short exposure it is possible to achieve deep detection limits, thanks to the very low ACIS background and sharp point spread function (PSF) of the telescope (Garmire et al. 2003). Most of the pulsars reported here were observed in the course of our guaranteed observation time (GTO) program (PI G. Garmire) with ≈ 10 ks ACIS exposures. The rest of the data were taken from the *CXC* archive⁵. In the sample of 23 pulsars, 12 are detected by *Fermi* LAT and listed in the 2FGL catalog (The Fermi-LAT Collaboration 2011) or reported elsewhere. We also made use of KP08 and Pavlov et al. (2007) to include previously reported results. In Section 2 we describe how we measure the fluxes and their upper limits. In Section 3 we provide the measured parameters for each pulsar, as well as derived quantities such as X-ray luminosities and efficiencies. These results are discussed in Section 4, where we combine our findings with the previous results in the X-ray range and compare these with the γ -ray properties. Finally, we present our conclusions in Section 5.

2. OBSERVATIONS AND ANALYSIS

The fields of 23 pulsars were imaged with the ACIS I-array or S-array, with exposure times of typically 10 ks, as part of our GTO program, between 2001 and 2011. The data for each observation were processed using the standard pipeline. We filtered the pipeline-produced event lists, keeping only photons with energies 0.5–8 keV, and searched for X-ray sources in the vicinity of the known pulsar coordinates (see Figure 1). The coordinates, taken from the most recent ATNF catalog Manchester et al. (2005), typically should have subarc-second uncertainties (although there can be exceptions, see e.g., Kargaltsev et al. 2007). The final positional uncertainty region in the image is the combination of the ATNF coordinate uncertainty with the typical *Chandra* pointing error, $0''.6$ at 90% confidence. We then searched for significant X-ray detections within this area in each ACIS image.

We consider a target detected when, for N detected counts, the probability of finding $\geq N$ events by chance within a chosen aperture is less than 0.0001 ($\approx 4\sigma$). For Poisson statistics, this probability is given by

$$P(N, \lambda) = 1 - e^{-\lambda} \sum_{i=0}^{N-1} \frac{\lambda^i}{i!}, \quad (1)$$

⁵ <http://cxc.harvard.edu/cda/>

where λ is the average number of background counts in the source aperture. In observations where a source was seen within the search area, we placed our measurement apertures at the centroid of the photon distribution; in the case of no detection, we placed our aperture at the centre of the search region. In each case the background was measured in much larger regions free of sources, but located on the same chip.

For our short exposures, the numbers of detected photons are typically too small to perform a reliable spectral fitting. Therefore, we adopted a more straightforward approach to estimate the observed fluxes. We used the CIAO task `psextract` to calculate the effective area, $A(E_i)$, at a given energy E_i of the detected photon, at the position of the source. The observed flux and its uncertainty were then estimated following Pavlov et al. (2009):

$$f = T_{\text{exp}}^{-1} \sum_i E_i A(E_i)^{-1}, \quad (2)$$

$$\delta f = T_{\text{exp}}^{-1} \left[\sum_i E_i^2 A(E_i)^{-2} \right]^{1/2}, \quad (3)$$

where E_i is the energy of the i th photon and T_{exp} is the exposure time (the sum of good times corrected for deadtime). We measured the flux in both an $r = 1''$ aperture, appropriate for point sources (it contains $\approx 93\%$ of the point source flux for photons with $E = 1$ keV) and in an $1'' \leq r \leq 3''$ annulus, to measure possible extended emission from a compact PWN. We subtracted 5% of the point source flux due to the wings of the PSF within the $1'' \leq r \leq 3''$ annulus.

In the case of non-detection, there is no an even crude measure of the spectrum to use in Equations (2) and (3). Therefore, to calculate an upper limit, we calculate the number of counts corresponding to $P(N, \lambda) = 0.1$ (i.e., establishing a 90% confidence limit) for the measured background rate, and use `webPIMMS`⁶ to calculate the equivalent flux in the 0.5–8 keV band for a typical pulsar spectrum (a power-law with photon index $\Gamma=1.5$ and galactic absorption column appropriate to each source; see Section 3).

3. RESULTS

The immediate results of our analysis are summarize in Table 1 (detections) and Table 2 (non-detections). Although the detection significance is high for every source in Table 1, the flux measurements can be rather uncertain. For instance, it may be that several low- or mid-energy photons establish the detection, but the measured flux is dominated by a single high-energy photon (where the detector is much less sensitive). In such cases the flux uncertainty will be of the order of the measured flux.

The only dubious case is B1822–14, which has an excess of counts over the background in both data-sets but no apparent point-like source. The excess counts could, in principle, be due to a PWN with an approximate flux of $3 \times 10^{-15} \text{ erg s}^{-1} \text{ cm}^{-2}$, close to the limit we derive. Although two significant X-ray sources happen to fall on the same S3 chip, their positions are inconsistent with

⁶ <http://heasarc.nasa.gov/Tools/w3pimms.html>

that of B1822–14, and both sources have 2MASS counterparts. Also, one additional ATNF pulsar is in the field (J1837–0604), which does not have an X-ray counterpart. It is included as a non-detection in Table 2.

Note that there are faint X-ray sources in the vicinity of PSRs J1105–6107 and J1730–3350, but in both cases they are too far away to be acceptable pulsar counterparts.

Table 3 lists the dispersion measure (DM), spin-down luminosity \dot{E} , and distance d , of the pulsars, taken from the ATNF catalog⁷. Using these values, we can estimate the absorption column, $N_{\text{H}} = 3.1 \times 10^{19} \text{DM cm}^{-2}$ (assuming an average 10% degree of ionization along the line of sight), unabsorbed flux, luminosity, and efficiency.

For three pulsars, J1958+2846, J1413–6205 and J1023–5746, DM is not known. In these cases we assumed a distance based on the position of the most prominent spiral arms in the direction to the pulsar, and corresponding extinction values. The calculated luminosity and efficiency values must therefore be taken with particular caution.

4. DISCUSSION

By adding the flux measurements or upper limits for 23 pulsars observed with *Chandra* ACIS we have significantly expanded the sample of pulsars analyzed by KP08. In Figure 2 (top panel) we plot the pulsar luminosity, $L_{\text{X}}^{\text{psr}}$, versus spin-down power \dot{E} . One can see that, in general, $L_{\text{X}}^{\text{psr}}$ increases with \dot{E} , in agreement with the previously noticed trends (e.g., Seward & Wang 1988; Becker & Trümper 1997; Possenti et al. 2002; Cheng et al. 2004; Li et al. 2008; KP08). However, the correlation is rather weak, and, because of the very large dispersion, it cannot be meaningfully described by a simple dependence $L_{\text{X}}^{\text{psr}}(\dot{E})$. The large scatter is also manifest in X-ray efficiencies, $\eta_{\text{X}}^{\text{psr}} = L_{\text{X}}^{\text{psr}}/\dot{E}$, which range from $\sim 10^{-5.5}$ to $\sim 10^{-1.8}$ in Figure 2 (top). For instance, such well-known pulsars as the Crab and B0540–69 are very efficient, while the very young, high- \dot{E} pulsar J2022+3842, recently discovered by Arzoumanian et al. (2011), has $\eta_{\text{X}}^{\text{psr}} = 10^{-5}$ (for a plausible $d = 8$ kpc). Similarly large variations in $\eta_{\text{X}}^{\text{psr}}$ are seen at lower \dot{E} down to $\dot{E} \sim 10^{36} \text{ erg s}^{-1}$.

An obvious cause of the scatter could be incorrectly determined distances for some of the pulsars. However, for majority of them (including J2022+3842), the distances cannot be wrong by more than a factor of a few, too little to explain the scatter. One can allude to the beaming of the magnetospheric radiation as another possible factor contributing to the spread in $\eta_{\text{X}}^{\text{psr}}$. However, the X-ray efficiencies of PWNe accompanying many of these pulsars show a similarly large scatter (see Figure 1 in KP10), although the PWN emission is not expected to be substantially beamed. In several cases neither pulsar nor PWN were detected, including the most X-ray underluminous PSR J1913+1011, for which $\eta_{\text{X}}^{\text{psr}} + \eta_{\text{X}}^{\text{pwn}} < 5.8 \times 10^{-6}$. (Note, that the limit also includes any thermal pulsar emission and compact PWN contribution, which means that the actual limit on the nonthermal magnetospheric emission must be even lower.) Therefore, the lack of

tight correlation between the $L_{\text{X}}^{\text{psr}}$ and \dot{E} can hardly be explained just by the beaming and poorly known distances.

Despite the huge scatter, the *maximum upper bound* on $L_{\text{X}}^{\text{psr}}$ at given \dot{E} appears to be well defined. For $\dot{E} \gtrsim 10^{35} \text{ erg s}^{-1}$ it approximately follows $L_{\text{X,crit}}^{\text{psr}} \propto \dot{E}^{1.6}$ (dashed line in Figure 2, top panel); however, for $\dot{E} \lesssim 10^{34} \text{ erg s}^{-1}$ the dependence on \dot{E} seems to flatten to $\propto \dot{E}^{2/3}$ or even flatter (Posselt et al. 2012).

Both the extreme scatter and the existence of the upper bound suggest that additional parameters must enter in the $L_{\text{X}}^{\text{psr}}(\dot{E}, \dots)$ dependences. One possibility is that there may be two qualitatively different emission regimes which correspond to two distinct $L_{\text{X}}^{\text{psr}}(\dot{E})$ (e.g., those shown by the dashed and dash-dotted lines in Figure 2, top panel). Given all the uncertainties mentioned above, the current data could be consistent with such a dichotomy although other alternatives, such as a continuous dependence of $\eta_{\text{X}}^{\text{psr}}$ on some parameter, are also possible. This parameter, however, is unlikely to be just the angle between the magnetic dipole and pulsar spin axis because the orthogonal rotator B0906–49 (Kramer & Johnston 2008) has an unremarkable X-ray efficiency compared to other pulsars with similar \dot{E} . One can also speculate that for low- \dot{E} pulsars the PWN becomes so compact that it is cannot be resolved even with *CXO*. A larger sample of pulsars with well known distances and good quality spectra is required to discriminate between the various alternatives. Also, the measurements of pulsed non-thermal emission can be used to constrain the very compact PWN contribution.

It is interesting to compare the $L_{\text{X}}^{\text{psr}}$ vs. \dot{E} correlation with that seen in γ -rays. Abdo et al. (2010) have presented the first analysis of the properties of 46 pulsars detected by *Fermi* LAT. Shortly afterwards, more *Fermi* pulsars were discovered (Saz Parkinson et al. 2010; Pletsch et al. 2012). We have calculated the > 0.1 GeV luminosities of the 54 γ -ray pulsars using the published⁸ pulsar fluxes and the best published estimates of the distances. Figure 2 (bottom panel) shows the correlation between the γ -ray luminosity, L_{γ}^{psr} , and \dot{E} (cf. Figure 2 in Marelli et al. 2011). The correlation between L_{γ}^{psr} and \dot{E} appears to be tighter than that between $L_{\text{X}}^{\text{psr}}$ and \dot{E} (despite the presumably stronger beaming in γ -rays as follows from higher pulsed fractions; Abdo et al. 2010), and it also differs in shape from the $L_{\text{X}}^{\text{psr}}$ vs. \dot{E} correlation⁹ (cf. top and bottom panels in Figure 2). For the energetic pulsars ($\dot{E} \gtrsim 10^{35} \text{ erg s}^{-1}$) the L_{γ}^{psr} vs. \dot{E} correlation appears to be consistent with the expected $\dot{E}^{1/2}$ law (e.g., Harding 1981), or with an even flatter one (see $L_{\gamma}^{\text{psr}} \propto \dot{E}^{1/3}$ line in Figure 3, bottom). However, at lower \dot{E} the observed correlation is more consistent with an $L_{\gamma}^{\text{psr}} \propto \dot{E}$ scaling, implying a break around $\dot{E} \sim 10^{35} \text{ erg s}^{-1}$ in the $L_{\gamma}^{\text{psr}}(\dot{E})$ dependence. The break hints at a qualitative change either in the emission

⁸ If no published flux values were found, we took them from the 2FGL catalog (The Fermi-LAT Collaboration 2011).

⁹ Note that the vertical axis range is the same in both panels of

⁷ <http://www.atnf.csiro.au/research/pulsar/psrcat/expert.html> Figure 2.

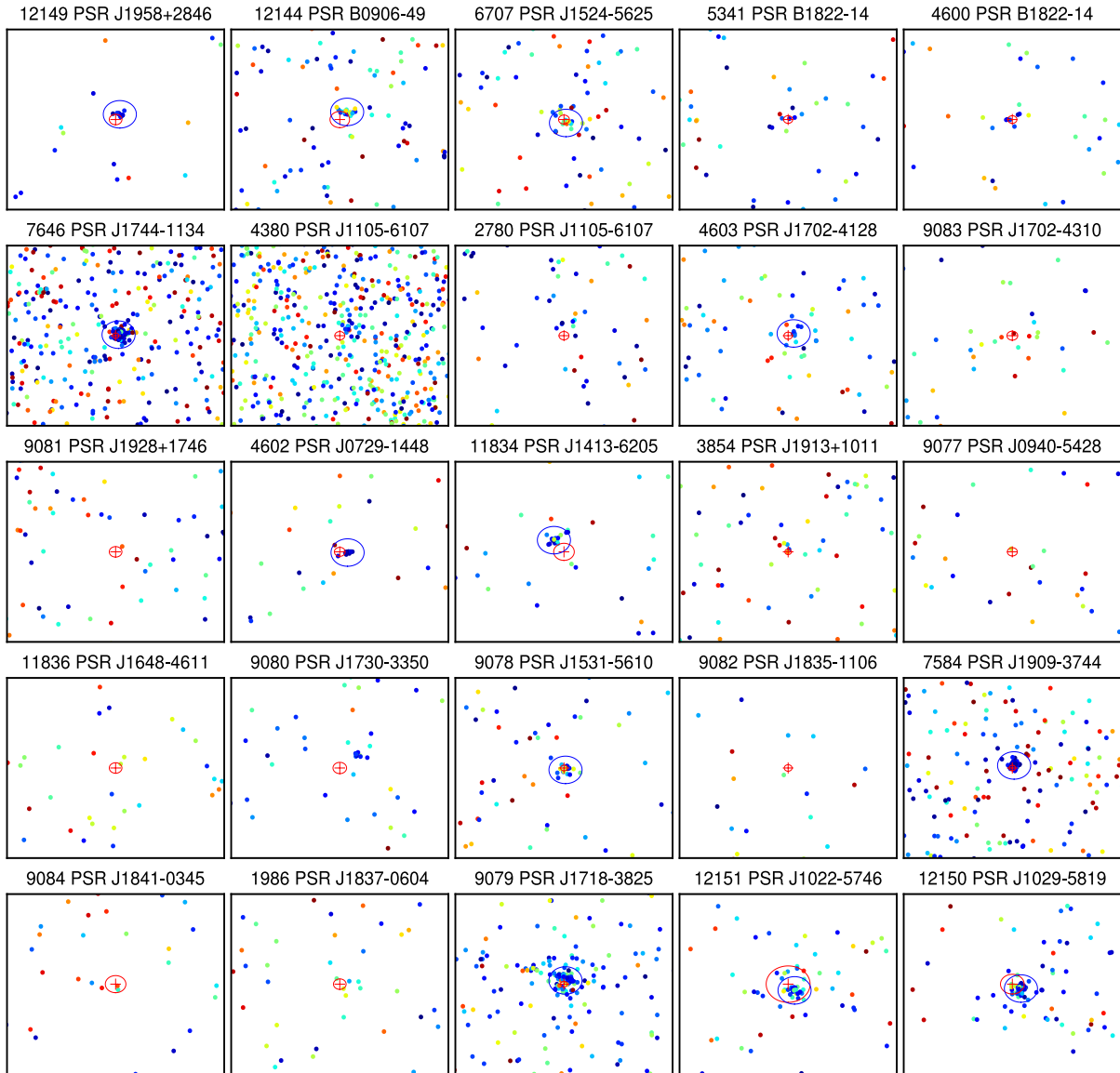


FIG. 1.— Scatter plots showing the distributions of photons and their energies for the pulsar fields. Each panel is $40'' \times 40''$. North is up, East is to the left. The positional uncertainties are shown by red circles (centred on the ATNF pulsar positions shown by the red crosses); a $3''$ aperture is shown for detected sources. Each photon is color coded according to its energy.

mechanism or in the spectral energy distribution (SED) of the primary particles (see below). Such a break was expected to occur at somewhat lower $\dot{E} \simeq 10^{33}$ erg s $^{-1}$ in the polar cap model (Harding et al. 2002). However, recent simulations based on the slot gap model seem to predict a break in the $L_{\gamma}^{\text{psr}} - \dot{E}$ relationship at $\dot{E} \simeq 10^{35}$ erg s $^{-1}$ (see Figure 1 in Pierbattista et al. 2011). It is more difficult to determine how the break in the primary particle SED will affect the properties of the secondary electrons and their synchrotron emission (see below), but some impact is likely, and it could be seen in the $L_{\text{X}}^{\text{psr}} - \dot{E}$ relationship (Figure 2, top panel) and in the multiwavelength spectra. Indeed, there is an intriguing coincidence between the values of \dot{E} at which the $L_{\text{X,crit}}^{\text{psr}} - \dot{E}$ and $L_{\gamma}^{\text{psr}} - \dot{E}$ appear to exhibit a break, although the slopes change

in the opposite ways. Also, the L_{γ}^{psr} vs. \dot{E} correlation is significantly stronger (i.e., the scatter is weaker) than the $L_{\text{X}}^{\text{psr}}$ vs. \dot{E} correlation.

The comparison of the top and bottom panels in Figure 2 makes it obvious that while the X-ray and γ -ray efficiencies can be similar for some very young pulsars, older pulsars are generally more efficient γ -ray emitters. This can also be seen in Figure 3, where we plot the distance-independent X-ray to γ -ray luminosity ratio for gamma-ray pulsars observed in X-rays. Although the scatter is large (mainly due to that in $L_{\text{X}}^{\text{psr}}$), the ratio increases with decreasing \dot{E} down to $\dot{E} \simeq 10^{35}$ erg s $^{-1}$, at which point the trend appears to reverse. These results suggest \dot{E} -dependent changes in the shapes of the multiwavelengths (MW) spectra of pulsars. Perhaps, it

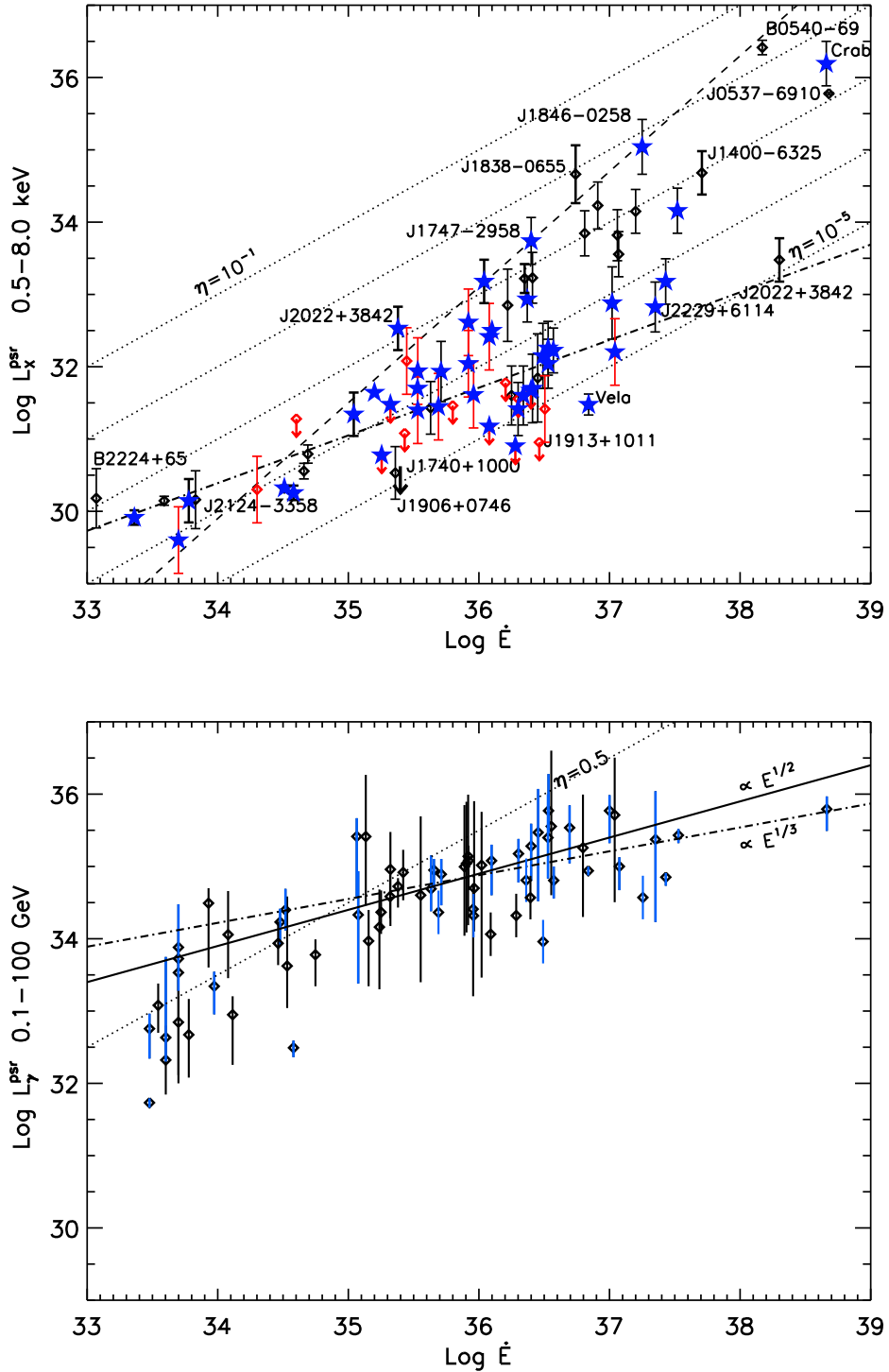


FIG. 2.— The top panel shows non-thermal X-ray luminosity vs. spin-down power \dot{E} . The dashed and dash-dotted lines corresponds to $L_X \propto \dot{E}^{1.6}$ and $L_X \propto \dot{E}^{2/3}$, respectively (see text for discussion). The constant efficiency ($\eta = L/\dot{E}$) lines are shown by the dotted lines. The downward arrows show 90% confidence upper limits. The blue stars mark γ -ray pulsars. The red errorbars and limits are from this paper, the rest are taken from KP08. The bottom panel shows γ -ray luminosity (in 0.1–100 GeV) vs. pulsar's \dot{E} . X-ray detected pulsars are shown in blue.

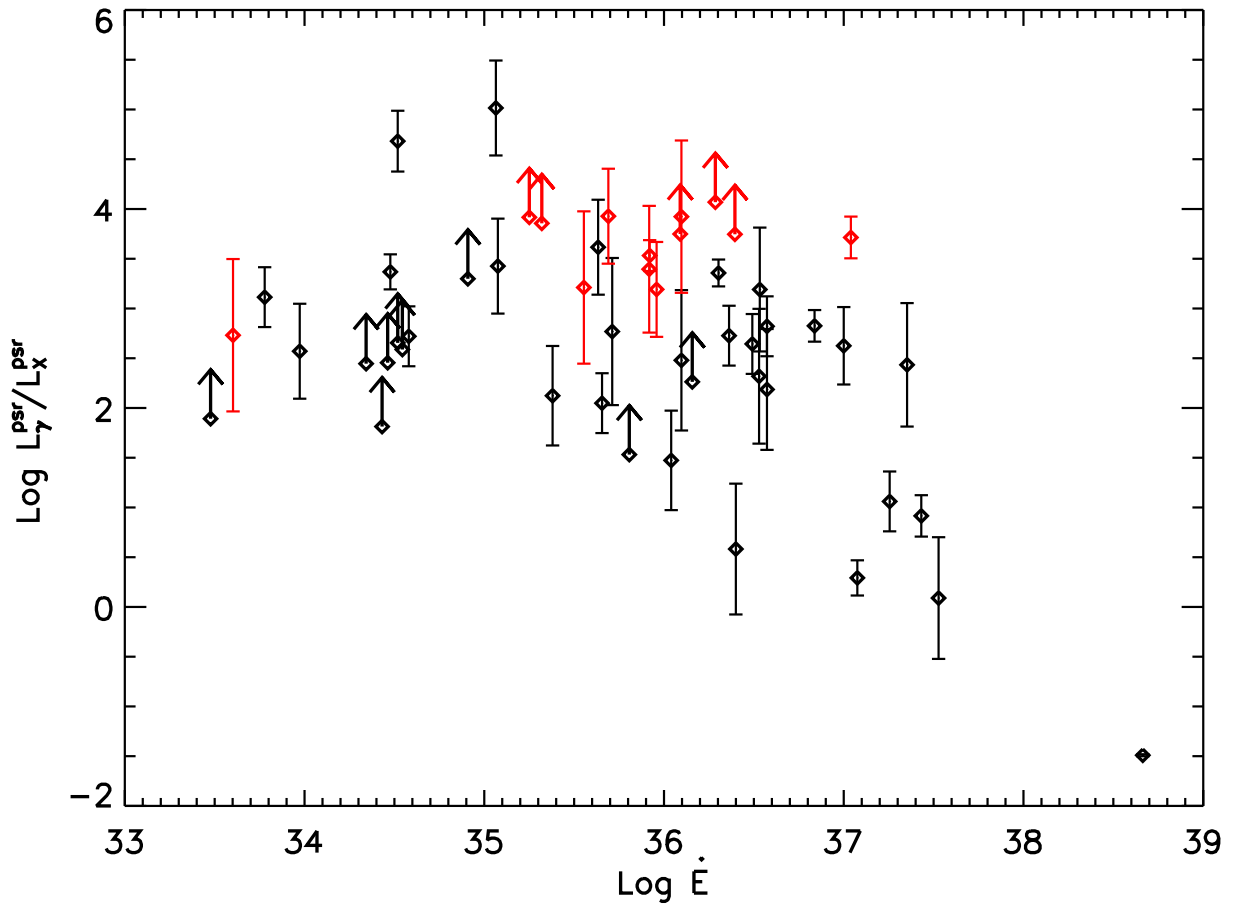


FIG. 3.— X-ray to γ -ray flux ratios for *Fermi*/LAT-detected pulsars that have been observed with *CXO*/ACIS. The ratio is independent of distances, which are poorly known for many pulsars. The pulsars analyzed in this paper are shown in red.

could be a change in the slope of a broadband power-law (PL) spectrum (if one attempts to describe most of MW emission as a curved or broken PL) or more complex changes. To better understand the implications of our findings for the magnetospheric models, a larger number of γ -ray pulsars with $\dot{E} = 10^{33} - 10^{35} \text{ erg s}^{-1}$ should be observed in X-rays with long enough exposures to either detect their X-ray emission or set restrictive upper limits.

It is generally believed that the pulsar GeV emission is produced by the curvature radiation of primary electrons pulled from the neutron star (NS) surface and accelerated by the electric field component parallel to the magnetic field. The curvature photons initiate pair cascades leading to the production of secondary or higher-generation electrons that emit synchrotron radiation at lower frequencies (optical to X-rays; e.g., Cheng et al. 1998; Harding 2008, 2009, and reference therein). In the high-altitude slot-gap and outer-gap models the primary particles keep accelerating up to 10–100 NS radii, gain momentum transverse to the magnetic field via resonant cyclotron absorption (Lyubarskii & Petrova 1998), and emit significant synchrotron radiation up to MeV (and possibly even GeV) energies in young pulsars (e.g., Baring 2011). Within this framework, it is still possible to have a MW (from optical to GeV) spectrum whose shape would resemble a single broadband PL with a cut-off at the highest energies (Takata et al. 2008), which seems to be in qualitative agreement with MW spectra of some pulsars (Durant et al. 2011). However, additional processes, such as the modification of the spectrum by inverse Compton scattering (Harding 2008) or by synchrotron self-Compton process (Zhang & Cheng 2002), can play important role under certain conditions. Our findings imply that the relative contributions of these processes may vary, depending on the geometry of the magnetosphere or the \dot{E} magnitude.

5. SUMMARY

By analyzing the population of rotation-powered pulsars detected by *CXO*, we found that the $L_X^{\text{psr}}-\dot{E}$ relationship cannot be meaningfully described as a simple $L_X^{\text{psr}}(\dot{E})$ dependence. There is some degree of correlation between L_X^{psr} and \dot{E} , but the extreme scatter (by > 4 orders of magnitude) in the X-ray radiative efficiencies is present for pulsars with $\dot{E} \gtrsim 10^{36} \text{ erg s}^{-1}$. Although existing data hint that the scatter may decrease with decreasing \dot{E} , perhaps becoming substantially smaller at $\dot{E} \lesssim 10^{35} \text{ erg s}^{-1}$, this could simply be the result of small-number statistics (few pulsars with low \dot{E} have been detected) and of the limited sensitivity of existing observations. The reasons for the scatter are unclear. The deepest X-ray limits reported in this paper strongly support the idea that L_X^{psr} depends not only on \dot{E} but also strongly depends on other parameters. At the same time, it seems that the upper bound on the $L_X^{\text{psr}}-\dot{E}$ relationship is fairly well defined ($L_{X,\text{crit}}^{\text{psr}} \propto E^{1.6}$), corresponding to such values of the “hidden” parameters that deliver maximum radiative efficiency at a given \dot{E} .

We thank Brian Newman who participated in the initial stages of this work. The comparison with a sample of γ -ray pulsars detected by *Fermi* LAT shows that the correlation between L_γ^{psr} and \dot{E} is much tighter, but again it can hardly be described by a simple power-law $L_\gamma^{\text{psr}}(\dot{E})$ dependence. The break between $\dot{E} \sim 10^{34}$ and $10^{35} \text{ erg s}^{-1}$ is suggested by the existing data. Intriguingly, a break in $L_{X,\text{crit}}^{\text{psr}}-\dot{E}$ is at similar \dot{E} values.

The work on this project was partly supported through the NASA grants NNX06AG36G, NNX09AC81G and NNX09AC84G, and National Science Foundation grants No. AST0908733 and AST0908611. The work by G. G. P. was partly supported by the Ministry of Education and Science of the Russian Federation (contract 11.634.31.0001).

REFERENCES

- Abdo, A. A., et al. 2010, *ApJs*, 187, 460
 Arzoumanian, Z., Gotthelf, E. V., Ransom, S. M., Safi-Harb, S., Kothes, R., & Landecker, T. L. 2011, *ApJ*, 739, 39
 Baring, M. G. 2011, in *American Institute of Physics Conference Series*, Vol. 1379, American Institute of Physics Conference Series, ed. E. Göğüş, T. Belloni, Uuml. Ertan, 74–81
 Becker, W., & Trümper, J. 1997, *AAP*, 326, 682
 Cheng, K. S., Gil, J., & Zhang, L. 1998, *ApJ*, 493, L35
 Cheng, K. S., Taam, R. E., & Wang, W. 2004, *ApJ*, 617, 480
 Durant, M., Kargaltsev, O., & Pavlov, G. G. 2011, *ApJ*, 743, 38
 Garmire, G. P., Bautz, M. W., Ford, P. G., Nousek, J. A., & Ricker, Jr., G. R. 2003, in *Society of Photo-Optical Instrumentation Engineers (SPIE) Conference Series*, Vol. 4851, Society of Photo-Optical Instrumentation Engineers (SPIE) Conference Series, ed. J. E. Truemper & H. D. Tananbaum, 28–44
 Harding, A. K. 1981, *ApJ*, 245, 267
 Harding, A. K. 2008, in *American Institute of Physics Conference Series*, Vol. 968, *Astrophysics of Compact Objects*, ed. Y.-F. Yuan, X.-D. Li, & D. Lai, 104–111
 Harding, A. K. 2009, in *Astrophysics and Space Science Library*, Vol. 357, *Astrophysics and Space Science Library*, ed. W. Becker, 521
 Harding, A. K., Muslimov, A. G., & Zhang, B. 2002, *ApJ*, 576, 366
 Kargaltsev, O., & Pavlov, G. G. 2008, in *American Institute of Physics Conference Series*, Vol. 983, *40 Years of Pulsars: Millisecond Pulsars, Magnetars and More*, ed. C. Bassa, Z. Wang, A. Cumming, & V. M. Kaspi, 171–185 (KP08)
 Kargaltsev, O., & Pavlov, G. G. 2010, in *American Institute of Physics Conference Series*, Vol. 1248, *American Institute of Physics Conference Series*, ed. A. Comastri, L. Angelini, & M. Cappi, 25–28 (KP10)
 Kargaltsev, O., Pavlov, G. G., & Garmire, G. P. 2007, *ApJ*, 660, 1413
 Kramer, M., & Johnston, S. 2008, *MNRAS*, 390, 87
 Li, X.-H., Lu, F.-J., & Li, Z. 2008, *ApJ*, 682, 1166
 Lyubarskii, Y. E., & Petrova, S. A. 1998, *A&A*, 337, 433
 Manchester, R. N., Hobbs, G. B., Teoh, A., & Hobbs, M. 2005, *AJ*, 129, 1993
 Marelli, M., De Luca, A., & Caraveo, P. A. 2011, *ApJ*, 733, 82
 Pavlov, G. G., Kargaltsev, O., Garmire, G. P., & Wolszczan, A. 2007, *ApJ*, 664, 1072
 Pavlov, G. G., Kargaltsev, O., Wong, J. A., & Garmire, G. P. 2009, *ApJ*, 691, 458
 Pierbattista, M., Grenier, I., Harding, A., & Gonthier, P. L. 2011, in *American Institute of Physics Conference Series*, Vol. 1357, *American Institute of Physics Conference Series*, ed. M. Burgay, N. D’Amico, P. Esposito, A. Pellizzoni, & A. Possenti, 249–252
 Pletsch, H. J., et al. 2012, *ApJ*, 744, 105
 Posselt, B., Pavlov, G. G., Manchester, R. N., Kargaltsev, O., & Garmire, G. P. 2012, submitted to *ApJ*

Possenti, A., Cerutti, R., Colpi, M., & Mereghetti, S. 2002, AAP, 387, 993
Saz Parkinson, P. M., et al. 2010, ApJ, 725, 571
Seward, F. D., & Wang, Z.-R. 1988, ApJ, 332, 199
Takata, J., Chang, H.-K., & Shibata, S. 2008, MNRAS, 386, 748

The Fermi-LAT Collaboration. 2011, ArXiv e-prints
Zhang, L., & Cheng, K. S. 2002, ApJ, 569, 872

TABLE 1
 PULSAR DETECTIONS.

Object	ObsID	T_{exp} ks	Chip	R.A. deg	decl. deg	$N_{\text{ph}}(1'')$	\tilde{E} keV	$N_{\text{ph}}(3'')$	$N_{\text{ph}}^{\text{bg}}(1'')$	$F_{\text{X,obs}}^{\text{psr}}$	$F_{\text{X,obs}}^{\text{pwn}}$
PSR J1958+2846	12149	9.9	2	299.66672	+28.76531	10	1.3	12	0.1	13.6±4.4	4.0±3.0
PSR B0906-49	12144	34.6	3	137.14747	-49.21801	10	2.9	17	0.4	4.2±1.6	3.4±1.5
PSR J1524-5625	6707	13.7	7	231.20756	-56.42337	9	3.9	16	0.4	14.4±6.1	24±19
PSR J1744-1134	7646	63.3	7	266.12236	-11.58179	273	1.1	312	1.6	16.8±1.1	13.8±6.6
PSR J1702-4128	4603	10.4	7	255.71846	-41.47992	8	2.2	13	0.3	22.4±17.1	11.9±9.1
PSR J0729-1448	4602	4.1	7	112.31814	-14.81026	13	0.9	15	0.2	10.2±2.9	64±63
PSR J1413-6205	11834	9.9	0	213.37566	-62.09318	8	1.5	14	0.1	8.9±3.7	7.2±3.4
PSR J1531-5610	9078	9.9	3	232.86615	-56.18206	11	1.9	17	0.1	34.0±22.8	8.2±3.8
PSR J1909-3744	7584	29.7	7	287.44754	-37.73717	64	1.0	71	0.8	7.9±1.0	0.9±0.3
PSR J1718-3825	9079	9.9	3	259.55642	-38.42146	36	1.6	79	0.2	43.9±11.1	72±24
PSR J1022-5746	12151	9.9	3	155.76147	-57.76843	24	2.9	35	0.1	31.4±7.2	14.7±4.9
PSR J1028-5819	12150	9.9	2	157.11584	-58.31837	45	1.2	61	0.1	40.9±7.4	19.3±5.5

NOTE. — Chips 0–3 are ACIS-I chips, and chip 7 is ASIC-S3. $N_{\text{ph}}(1'')$ is the number of counts within the $r = 1''$ circle centered on the X-ray source, and \tilde{E} is the median energy of these photons. Positional uncertainties of the X-ray sources are dominated by the *Chandra* pointing error ($0''.3$ at 68% confidence). $N_{\text{ph}}(3'')$ is the number of counts in the $r = 3''$ circle. $N_{\text{ph}}^{\text{bg}}(1'')$ is the expected mean number of background counts scaled to the $r = 1''$ aperture. $F_{\text{obs}}^{\text{psr}}$ and $F_{\text{obs}}^{\text{pwn}}$ are the observed (absorbed) pulsar and PWN fluxes in the 0.5–8 keV band, in units $10^{-15} \text{ erg s}^{-1} \text{ cm}^{-2}$. $F_{\text{obs}}^{\text{pwn}}$ is the observed flux in the $1'' \leq r \leq 3''$ annulus, after subtracting the flux due to the point source.

 TABLE 2
 PULSAR NON-DETECTIONS.

Object	ObsID	T_{exp} (ks)	Chip	R.A.	decl.	$N_{\text{ph}}(3'')$	$N_{\text{ph}}^{\text{bg}}(3'')$	$F_{\text{X,u.l.}}$
PSR B1822-14	5341	18.0	0	276.26220	-14.78127	7	1.9	3.7
PSR B1822-14	4600	11.0	0	276.26220	-14.78127	6	1.1	3.0
PSR J1105-6107	4380 ^a	11.7	7	166.35904	-61.13094	15	24	...
PSR J1105-6107	2780	11.6	7	166.35904	-61.13094	5	2.5	5.6
PSR J1702-4310	9083	9.6	3	255.61225	-43.17778	3	1.3	5.3
PSR J1928+1746	9081	9.9	3	292.17700	+17.77417	1	2.1	5.8
PSR J1913+1011	3854	19.5	7	288.33475	+10.18971	5	2.9	2.9
PSR J0940-5428	9077	10.0	3	145.24258	-54.47794	1	1.1	2.8
PSR J1648-4611	11836	10.0	2	252.09175	-46.18778	2	1.3	5.2
PSR B1727-33	9080	9.9	3	262.63566	-33.84428	1	1.7	4.8
PSR J1835-1106	9082	10.0	2	278.82620	-11.10419	1	1.2	4.2
PSR J1841-0345	9084	10.0	3	280.41117	-3.81183	3	1.3	4.4
PSR J1837-0604	1986	9.0	6	279.43146	-6.08028	4	1.5	5.1

NOTE. — The coordinates correspond to the radio pulsar positions from ATNF catalog Manchester et al. (2005). Chips 0–3 are ACIS-I, and chip 7 is ASIC-S3. $N_{\text{ph}}(3'')$ is the number of counts within the $r = 3''$ circle centered on the radio pulsar position. $N_{\text{ph}}^{\text{bg}}(3'')$ is the expected mean number of background counts scaled to $r = 3''$ circular aperture. $F_{\text{X,u.l.}}$ is the upper limit on the observed (absorbed) flux in the 0.5–8 keV range corresponding to 90% confidence limit (see Section 2), in units of $10^{-15} \text{ erg s}^{-1} \text{ cm}^{-2}$.

^{0 a} This observation does not provide a useful limit because it was affected by a high background.

TABLE 3
 PULSAR PARAMETERS.

Object	l deg	b deg	DM pc cm ⁻³	P ms	Age kyrs	$\dot{E}/10^{35}$ erg s ⁻¹	$N_{\text{H}}/10^{21}$ cm ⁻²	d kpc	$F_{\text{X}}/10^{-15\text{a}}$ c.g.s.	$L_{\text{X}}/10^{31\text{b}}$ erg s ⁻¹	$\eta_{\text{X}}^{\text{c}}$	LAT ^d
PSR J1958+2846	65.88	-0.35	...	290	22	3.4	5 ^e	2 ^e	52	2.5	7.4×10^{-5}	Y
PSR B0906-49	270.27	-1.02	180	107	112	4.9	5.6	6.66	5.2	2.8	5.7×10^{-5}	Y
PSR J1524-5625	323.00	+0.35	153	78	32	32	4.7	3.84	15	2.6	8.1×10^{-6}	N
PSR J1744-1134	14.79	+9.18	3.14	4	7×10^6	0.05	0.1	0.42	17	0.04	8×10^{-5}	Y
PSR J1702-4128	344.74	+0.12	367	182	55	3.4	11.3	5.18	27	8.7	2.6×10^{-5}	N
PSR J0729-1448	230.39	+1.42	92	252	35	2.8	2.8	4.37	52	12	4.2×10^{-4}	N
PSR J1413-6205	312.37	-0.74	...	110	63	8.3	10 ^e	4 ^e	215	41.1	5.0×10^{-4}	Y
PSR J1531-5610	323.90	+0.03	111	84	97	9.1	3.4	3.10	36	4.1	4.5×10^{-5}	Y
PSR J1909-3744	359.73	-19.60	10.4	3	3×10^6	0.2	0.3	1.27	9.0	0.2	1×10^{-4}	N
PSR J1718-3825	348.95	-0.43	247	75	89	12	7.6	4.24	120	26	2.2×10^{-4}	Y
PSR J1023-5746	284.17	-0.41	...	111	46	110	15 ^e	4.5 ^e	64	16	1.5×10^{-5}	Y
PSR J1028-5819	285.06	-0.50	96	91	90	8.3	3.0	2.76	120	11	1.2×10^{-4}	Y
PSR B1822-14	16.81	-1.00	357	279	195	0.4	11.0	5.45	<5.5	<1.9	$<4.9 \times 10^{-4}$	N
PSR J1105-6107	290.49	-0.85	271	63	63	25	8.4	7.07	<7.9	<4.7	$<1.9 \times 10^{-5}$	Y
PSR J1702-4310	343.35	-0.85	377	240	17	6.3	11.6	5.44	<8.0	<2.9	$<4.5 \times 10^{-5}$	N
PSR J1928+1746	52.93	+0.11	177	69	82	16	5.5	8.13	<7.7	<6	$<3.8 \times 10^{-5}$	N
PSR J1913+1011	44.48	-0.17	179	36	169	29	5.5	4.48	<3.9	<0.9	$<3.3 \times 10^{-6}$	N
PSR J0940-5428	277.51	-1.29	134	87	42	19	4.2	4.27	<3.5	<0.8	$<4.0 \times 10^{-6}$	Y
PSR J1648-4611	339.44	-0.79	393	165	110	2.1	12.1	5.71	<7.8	<3.0	$<1.5 \times 10^{-4}$	Y
PSR B1727-33	354.13	+0.09	259	139	26	12	8.0	4.26	<6.6	<1.5	$<1.2 \times 10^{-5}$	Y
PSR J1835-1106	21.22	-1.51	133	166	128	1.8	4.1	3.08	<5.2	<0.6	$<3.4 \times 10^{-5}$	N
PSR J1841-0345	28.42	+0.44	194	204	56	2.7	6.0	4.15	<5.9	<1.2	$<4.5 \times 10^{-5}$	N
PSR J1837-0604	25.96	+0.26	462	96	34	20	14.3	6.19	<8.0	<3.6	$<1.9 \times 10^{-5}$	N

^{0 a} Unabsorbed flux in 0.5–8 keV for the point source (measured from $r = 1''$ circular aperture), corrected for the finite aperture size. For non-detections, the fluxes correspond to 90% confidence limits.

^{0 b} X-ray luminosity in 0.5–8 keV.

^{0 c} X-ray radiative efficiency $\eta_{\text{X}} = L_{\text{X}}/\dot{E}$.

^{0 d} *Fermi* LAT detection (Yes or No).

^{0 e} Crude estimates for the distance and N_{H} , to be regarded with caution.